

Analysis of systematic errors in the frequency-based approach to estimating the deuteron electric dipole moment in a frozen spin storage ring

Alexander Aksentev^{a,b,c,*}, Yury Senichev^b, Ereney Valetov^d

^a*Institut für Kernphysik (IKP-2), Forschungszentrum Jülich, Jülich, Germany*

^b*Institute for Nuclear Research of the Russian Academy of Sciences, Moscow, Russia*

^c*National Research Nuclear University "MEPhI," Moscow, Russia*

^d*Department of Physics and Astronomy, Michigan State University, MI 48824, USA*

Abstract

The purpose of the present work is to evaluate the capability of the frequency-based approach to the measurement of the electric dipole moment of a charged particle in a storage ring environment.

For that purpose, we analyzed several effects of the beam spin dynamics, which could result in systematic errors in the electric dipole moment estimator statistic. Those are: spin motion perturbations caused by betatron oscillations; spin decoherence in the frozen spin regime; properties of the magnetic dipole moment faking signal.

Keywords: electric dipole moment; frozen spin; spin transparency; spin dynamics; spin decoherence.

Contents

1	Introduction	2
2	The Frozen Spin concept	3
3	Effects of spin dynamics	6

*Corresponding author

Email addresses: alexaksentyev@gmail.com (Alexander Aksentev), y.senichev@inr.ru (Yury Senichev), eremey@valetov.com (Ereney Valetov)

3.1	Betatron oscillations	6
3.1.1	Problem statement	6
3.1.2	Simulation setup	7
3.1.3	Simulation results and conclusions	8
3.2	Spin decoherence	10
3.2.1	Origins	10
3.2.2	Theory behind the sextupole decoherence suppression	10
3.2.3	Sextupole field effect signatures	12
3.2.4	Decoherence suppression in an ideal lattice	13
3.2.5	Decoherence in an imperfect lattice	13
3.3	MDM faking signal	15
3.3.1	Problem statement	15
3.3.2	Results and conclusions	16
4	Conclusions	17

1. Introduction

The search for the electric dipole moments of elementary particles is motivated by the question of the baryon asymmetry of the universe. In his seminal 1967 paper [1] A. Sakharov proposed CP-symmetry violation as one of the conditions for baryogenesis. Permanent electric dipole moments (EDMs), if they exist, violate both the P- and T-symmetries, and hence, via the CPT-theorem, can be linked to CP-symmetry violation.

At the same time, the Standard Model (SM) predicts exceedingly small values for nucleon EDMs, in the range of 10^{-33} to 10^{-31} $e\cdot\text{cm}$, which is way below the current upper bound for the neutron EDM, with $d_n = 2.9 \cdot 10^{-26}$ $e\cdot\text{cm}$. This implies that particle EDMs can serve as a powerful tool for discovering physics beyond the SM. For example, CP-violations that are endemic in supersymmetric theories (SUSY) are such as to span d_n values in the range of 10^{-29} to 10^{-24} $e\cdot\text{cm}$. [2]

Up until now, all EDM-searching experiments were carried out with electrically-neutral particles, such as atoms or the neutron. The idea of searching of a charged particle's EDM in a storage ring environment appeared during the development of the g-2 experiment [3] in Brookhaven National Laboratory.

The original method proposal [4] consisted in observing a slow and gradual growth of the vertical component of polarization in an initially fully longitudinally-polarized beam injected into a storage ring in which spin precession due to the magnetic dipole moment (MDM) is suppressed. Since the MDM component of spin precession is assumed to be zero, the tilting of the polarization vector out of the orbit plane, which causes the growth of the vertical component, is an indication of the existence of something else that's turning the particles' spin-vectors. This something is presumed to be the EDM.

In the following, we will outline the frozen spin (FS) storage ring design concept, on which the methodology in reference [4] rests. Then, we will describe the characteristic features of the frequency-based approach to EDM measurements. After that, we will present the results of our analysis of the three major spin dynamics effects affecting the measurements.

2. The Frozen Spin concept

The dynamics of a spin vector \vec{s} in a magnetic field \vec{B} and an electrostatic field \vec{E} is described by the Thomas-BMT equation. Its generalized version, accounting for the effect of the particle's electric dipole moment, can be written in the rest frame as:

$$\frac{d\vec{s}}{dt} = \vec{s} \times \underbrace{(\vec{\Omega}_{MDM} + \vec{\Omega}_{EDM})}_{\vec{\Omega}_s}, \quad (1a)$$

where the magnetic (MDM) and electric (EDM) dipole moment angular velocities $\vec{\Omega}_{MDM}$ and $\vec{\Omega}_{EDM}$

$$\vec{\Omega}_{MDM} = \frac{q}{m} \left[G\vec{B} - \left(G - \frac{1}{\gamma^2 - 1} \right) \frac{\vec{E} \times \vec{\beta}}{c} \right], \quad (1b)$$

$$\vec{\Omega}_{EDM} = \frac{q}{m} \frac{\eta}{2} \left[\frac{\vec{E}}{c} + \vec{\beta} \times \vec{B} \right]. \quad (1c)$$

33 In the above equations, m , q , $G = (g - 2)/2$ are, respectively, the mass, charge,
 34 and anomalous magnetic moment of the particle; $\beta = v_0/c$ is its normalized
 35 speed; γ its Lorentz-factor. The EDM factor η is defined by the equation $d =$
 36 $\eta \frac{q}{2mc}$, in which d is the particle EDM, s its spin.

37 If the storage ring's radial electric field component [4, p. 10]

$$E_r = \frac{GB_y c \beta \gamma^2}{1 - G\beta^2 \gamma^2},$$

38 the MDM component in (1a) is set to zero: $\vec{\Omega}_{MDM} = \vec{0}$, and we are said to be
 39 operating in the frozen spin (also called “spin transparent”) regime.

40 In this case, the vertical polarization vector component is expected to be a
 41 harmonic signal

$$P_y = A \cdot \sin \left(\underbrace{\sqrt{(\omega_{edm} + \omega_{\langle E_v \rangle})^2 + \omega_y^2 + \omega_z^2}}_{\Omega} \cdot t + \delta \right), \quad (2)$$

42 where $\omega_{\langle E_v \rangle}$ denotes the MDM spin precession frequency generated by fields
 43 connected with machine imperfections. It is the primary source of systematic
 44 error in the storage ring EDM search experiment based on the classical, i.e. 3D,
 45 FS idea.

46 According to equation (2), two distinct measurement modes can be con-
 47 ceptualized in the FS measurement framework: *a)* the amplitude-, and *b)* the
 48 frequency-based methods.

49 The former is the classical 3D FS measurement methodology: all EDM-
 50 unrelated precession in the ring must first be suppressed; then, if the beam's
 51 polarization vector doesn't hold still, it indicates to us that something else (the
 52 EDM) exists that's turning it.

53 In the frequency-based methodology [5], on the other hand, spin precession
 54 is stopped only in the beam orbit plane, and the EDM indicator is the change
 55 to the vertical plane spin precession frequency under time reversal (the time
 56 reversal is simulated by reversing the beam circulation direction).

57 We call the state in which the beam particles' spins are frozen in the hori-
 58 zontal, but precess freely in the vertical, plane the 2D FS – or the spin wheel
 59 (SW) [6] – state. In view of this, the frequency-based methodology will also be
 60 referred to as the 2D Frozen Spin method.

61 Three advatages follow from not freezing the spin precession in the vertical
 62 plane:

- 63 (i) since we don't have to stop vertical plane MDM spin precession, lattice
 64 optical element alignment specifications aren't as stringent;
- 65 (ii) it also means that the spin precession axis is more stable, which is a remedy
 66 for another major systematic error – geometric phase;
- 67 (iii) and since we don't have to measure microradian deviations of the polar-
 68 ization vector from the beam orbit plane, the polarization measurement
 69 is much easier.

70 *The frequency-based methodology's characteristic features.* The frequency-based
 71 approach is characterized by two main features:

- 72 *a)* The existence of the EDM is inferred not from the change in the beam
 73 polarization vector's spatial orientation *itself*, but from the shift in the
 74 spatial orientation's *rate of change*;
- 75 *b)* The fields induced by machine imperfections, instead of being suppressed,
 76 are used as a spin wheel driver.
 - 77 • The spin wheel's roll direction is reversed by flipping the direction of
 78 the guide field;
 - 79 • its roll rate is controlled through observation of spin precession in the
 80 horizontal plane.

81 *Used terminology.* For terminology's sake, we should note that in the standard
 82 formalism one operates with the spin transfer matrix [7, p. 4]

$$\mathbf{t}_R = \exp(-i\pi\nu_s\vec{\sigma} \cdot \vec{n}) = \cos \pi\nu_s - i(\vec{\sigma} \cdot \vec{n}) \sin \pi\nu_s,$$

83 where $\nu_s = \Omega_s/\Omega_{cyc}$, the ratio of the particle's spin precession frequency to its
 84 cyclotron frequency, is termed *spin tune*, and \vec{n} , termed the *invariant spin axis*,
 85 defines the spin precession axis. They relate to the spin precession angular
 86 velocity as in

$$\vec{\Omega}_s = \omega_{cyc} \cdot \nu_s \vec{n}.$$

87 3. Effects of spin dynamics

88 3.1. Betatron oscillations

89 3.1.1. Problem statement

90 The problem of the betatron motion is as follows:

- a) the EDM statistic is composed from two estimates of the spin precession frequency; in one the EDM and MDM effects add up, in the other subtract:

$$\begin{cases} \hat{\omega}_{edm} &= \frac{1}{2}(\hat{\omega}_x^+ + \hat{\omega}_x^-), \\ \omega_x^\pm &= \omega_{edm} \pm \omega_{mdm}. \end{cases}$$

- 91 b) Those frequencies are estimated via fitting a harmonic function with con-
 92 stant parameters to polarimetry data:

$$f(t) = a \cdot \sin(\omega_x \cdot t + \delta) \mapsto \hat{\omega}_x,$$

93

$$(a, \omega_x, \delta) = \text{const.}$$

- 94 c) At the same time, the solution of the T-BMT equation for the vertical spin
 95 vector component has a non-constant amplitude $a = \sqrt{\bar{n}_x^2 + (\bar{n}_y \cdot \bar{n}_z)^2}$ for
 96 a betatron-oscillating particle.

3.1.2. Simulation setup

In the simulation we used a FS lattice with bent E+B-field spin rotators shown in Figure 1. We used an imperfect machine; imperfections were simulated by spin-rotator tilts about the optic axis. The tilt angles were normally-distributed, each trial the expectation of the tilt distribution was varied. The non-zero expectation value simulates the application of a spin wheel driver. Imperfections introduced in this way affect only the particle spin dynamics, leaving the orbital dynamics the same for every trial.

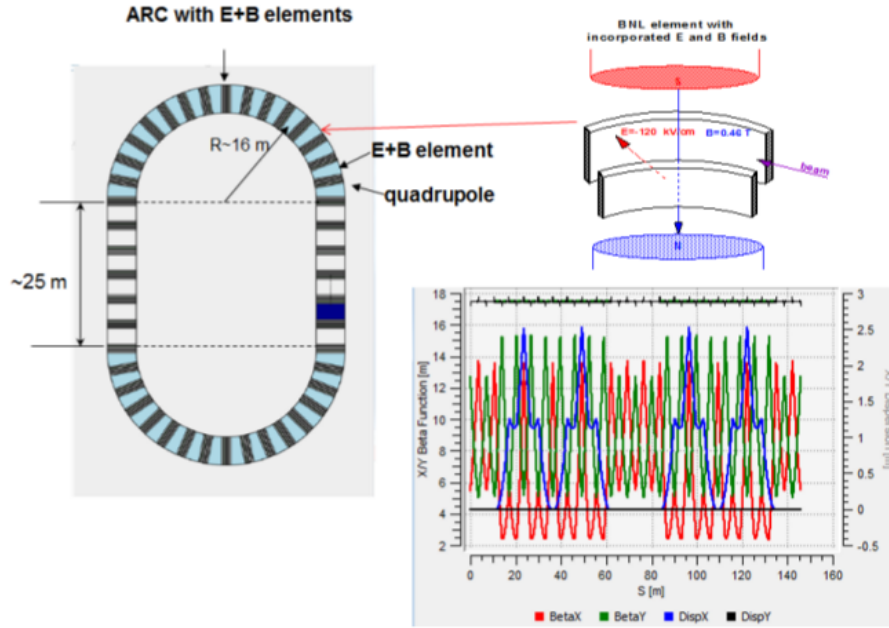


Figure 1: Frozen Spin lattice used in all simulations. Bent E+B-field spin-rotators are inserted into the arc sections. The lattice length is 146 m, the beam injection energy is 270 MeV. Image taken from [9].

Particles injected into the lattice were betatron-scillating in the vertical plane for the most part. Since 270 MeV is not exactly the FS energy¹ for this lattice,

¹The more precise value is 270.0092 MeV

107 the radial component of the spin precession axis is fairly small. This, however,
 108 does not pose a problem for this particular simulations, since it only amplifies
 109 the effect of vertical betatron oscillations, which were being studied.

110 In the analysis we used three data sets. The s_y^{trk} time series was taken
 111 directly from the COSY Infinity [8] tracker. The s_y^{gen} were data generated using
 112 a harmonic function with varying amplitude and frequency; the amplitude and
 113 frequency values at time t were computed based on the invariant spin axis and
 114 spin tune time series obtained during COSY Infinity tracking. The s_y^{idl} data
 115 series was also computed from the harmonic signal, but constant estimates of
 116 amplitude and frequency were used.

From the data series, two comparator statistics/residuals were computed:

$$\epsilon_1(t) = s_y^{gen}(t) - s_y^{idl}(t), \quad (\text{generator residual})$$

$$\epsilon_2(t) = s_y^{trk}(t) - s_y^{idl}(t). \quad (\text{tracker residual})$$

117 The tracker residual serves as an estimate of the amplitude oscillations
 118 caused by the particle's betatron motion, and hence it is the primary statis-
 119 tic for analysis.

120 3.1.3. Simulation results and conclusions

121 In Figure 2 are shown the time-dependencies of the comparator residuals.
 122 These are plots for the particle with the largest (3 mm) amplitude of betatron
 123 oscillations. We observe that even in this case the tracker residual's oscillation
 124 amplitude does not exceed 10^{-5} ; for a whole ensemble of particles, this value
 125 can only be smaller, due to the averaging effect.

126 The amplitude growth in the generator residual's case is due to the differ-
 127 ence between the ideal and generator signal's oscillation frequencies, which is a
 128 consequence of the way in which we defined the ideal signal's parameters.

129 Figure 3 presents the most significant simulation results. We make two
 130 observations:

- 131 (1) the comparator's standard deviations follow the same functional depen-
- 132 dence on the SW driver's strength as the spin tune's, and do not show any

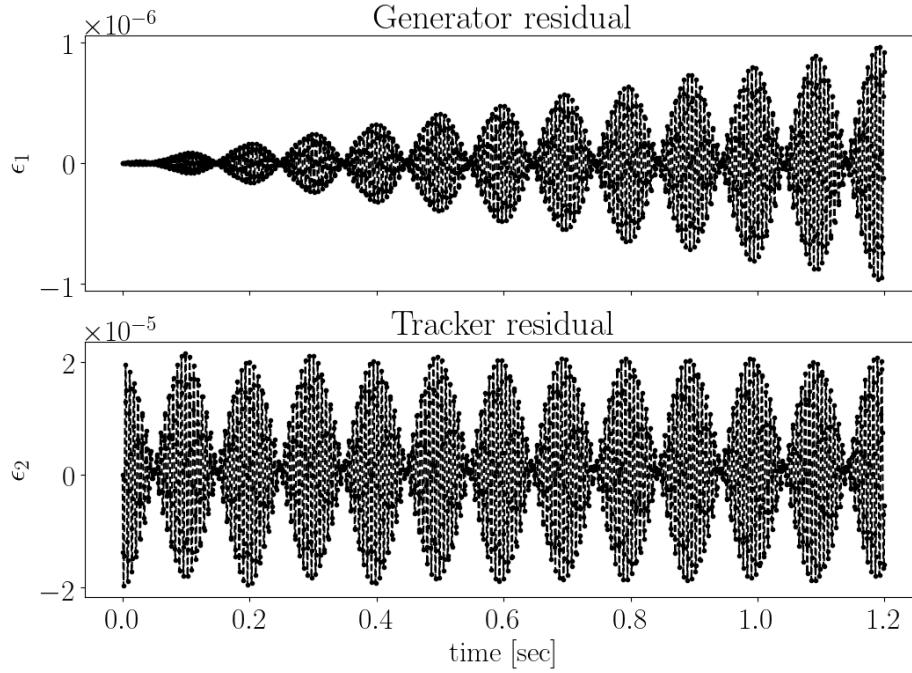


Figure 2: Comparator statistics' time-dependence.

interest in the behavior of the spin precession axis;

- (2) the variability of the precession axis grows smaller as the driver strength increases. This is what we referred to as advantage (ii) of the frequency-based approach.

This simulation was set up so as to check the robustness of the frequency-based approach's EDM statistic with regard to perturbations to the particle spin dynamics; specifically, those that cause the invariant spin axis to change its orientation. Even though the only source of perturbation we used was the particles' betatron motion, some general conclusions can be inferred from the results:

- (1) The amplitude oscillations are small, as evidenced by Figure 2 (directly), and the residual standard deviation plots in Figure 3a (indirectly). We expect the random polarization measurement error to occur at the percent

level, which means that the superposition of this systematic error with the random measurement error should not exhibit any statistically-significant systematicity.

(2) The correlation coefficient between the \hat{a} - and $\hat{\omega}_x$ -estimates is less than 10%. The measured signal's amplitude oscillations affect the amplitude estimate in the first place, while their effect on the frequency estimate is described by the correlation coefficient. Since it is small, even if our first conclusion is false, and the amplitude oscillations are sufficient to bias the \hat{a} -estimate, their effect on the frequency estimate will be attenuated by at least a factor of 10.

(3) This systematic effect is controllable. This can be observed in Figure 3b, where the precession axis' variability goes down with the SW roll rate. The frequency-based approach permits the application of a SW driver in a reasonably wide strength range.

3.2. Spin decoherence

3.2.1. Origins

According to equation $\nu_s = \gamma G$, a particle's spin tune depends on its energy. Because particles in a bunch travel different length orbits, their equilibrium energy levels also experience a dispersion. As a consequence, their spin vectors precess at different rates, which is the immediate cause of decoherence. [10]

In Figure 4a one can see the longitudinal phase space portraits of particles doing betatron oscillations in the vertical plane. The centers of the ellipses indicate the particles' equilibrium energy levels. Data used in the drawing of this figure was obtained in a simulation in which third-order spin and orbital transfer maps were utilized. Compare with the linear theory prediction, represented in Figure 4b.

3.2.2. Theory behind the sextupole decoherence suppression

Our hypothesis is that decoherence is a result of the dispersion in the particle equilibrium energy levels. If one solves the system of equations for the

175 longitudinal particle dynamics,² assuming a non-linear momentum compaction
 176 factor $\alpha = \alpha_0 + \alpha_1 \cdot \delta$, one will obtain the following general expression for the
 177 equilibrium level momentum shift:

$$\Delta\delta_{eq} = \frac{\gamma_0^2}{\gamma_0^2\alpha_0 - 1} \left[\frac{\delta_m^2}{2} (\alpha_1 - \alpha_0\gamma_0^{-2} + \gamma_0^{-4}) + \left(\frac{\Delta L}{L} \right)_\beta \right]. \quad (3)$$

178 In the above equation:

- 179 a) $\delta = \Delta p/p$ is the particle's momentum offset³;
- 180 b) γ_0 is the Lorentz factor of the reference particle;
- 181 c) $\left(\frac{\Delta L}{L} \right)_\beta = \frac{\pi}{2L} [\epsilon_x Q_z + \epsilon_y Q_y]$ is the orbit lengthening due to betatron oscil-
 182 lations;
- 183 d) $\epsilon_{x,y}$ are, respectively, the horizontal and vertical transverse emittances,
 184 $Q_{x,y}$ the corresponding betatron tunes.

185 The expression (3) contains two terms: the first has to do with the non-linear
 186 momentum compaction factor, the second with the particle orbit length.

If one inserts a sextupole of strength

$$S_{sext} = \frac{1}{B\rho} \frac{\partial^2 B_y}{\partial x^2} \quad (4)$$

into the beam line, its field will first of all affect the particle trajectories:

$$\left(\frac{\Delta L}{L} \right)_{sext} = \mp \frac{S_{sext} D_0 \beta_{x,y} \epsilon_{x,y}}{L}, \quad (5)$$

and second — it will modify the non-linear part of the momentum compaction factor:

$$\Delta\alpha_{1,sext} = -\frac{S_{sext} D_0^3}{L}. \quad (6)$$

187 We call equation (5) the orbit length effect, equation (6) the momentum com-
 188 paction factor effect. In the following sections we will try to analyze the signa-
 189 tures of these effects in spin tune data.

²For details, please cf. reference [11].

³ δ_m is the amplitude of synchrotron oscillations.

190 *3.2.3. Sextupole field effect signatures*

191 *Momentum compaction factor effect.* In Figure 5a is drawn the dependence of
192 a particle's mean spin tune level on its mean energy level. In this simulation
193 we injected an ensemble of particles with differing initial energy offsets on the
194 closed orbit of the FS lattice from Figure 1. Since the sextupole fields do not
195 affect the closed orbit, this simulation tests only for the momentum compaction
196 factor effect.

197 The plot exhibits two features:

- 198 (1) the functional dependence $\langle \nu_s \rangle (\langle \Delta K / K \rangle)$ changes with the field gradient;
199 (2) the point density distribution does not vary.

200 In Figure 5b we drew the particles' longitudinal phase space portraits. We
201 observe no change in the portraits when the sextupole field gradient is varied,
202 which is attributed to the particle orbit lengths' not changing.

203 *Orbit length effect.* In this simulation, particles were injected at the same initial
204 energy, but different vertical offsets from the closed orbit. Because of that,
205 they do betatron oscillations, and as a result, synchrotron oscillations. As a
206 consequence of equation (3), we should anticipate both sextupole field effects in
207 this simulation.

208 As predicted, Figure 6a exhibits two features:

- 209 (1) the functional dependence $\langle \nu_s \rangle (\langle \Delta K / K \rangle)$ changes as in the previous sim-
210 ulation;
211 (2) the point density distribution changes also.

212 In Figure 6b we see that the phase portraits compress when the sextupole
213 field gradient is changed. This compression corresponds to the point density
214 change, seen in Figure 6a.

215 *Conclusions.* The above analysis brought us to the following conclusions:

(1) The signature of the sextupole fields' momentum compaction factor effect is the change in the functional form of the mean spin tune dependence on the particle's mean energy level $\langle \nu_s \rangle (\langle \Delta K / K \rangle)$.

(2) The pure orbit length effect is the reduction in the dispersion of the mean energy levels.

Contrary to our original intuition, the minimization of the dispersion in the mean energy levels does not effect the desired minimization in the dispersion of the particles' spin tunes. In Figure 6a, for example, we see that the sextupole gradient value corresponding to the minimal $\sigma [\Delta K / K]$ is not optimal in terms of $\sigma [\langle \nu_s \rangle]$, while at the optimal value, the $\Delta K / K$ dispersion does not matter at all.

3.2.4. *Decoherence suppression in an ideal lattice*

In the lattice from Figure 1 three families of sextupoles are used: one is to reduce spin decoherence associated with horizontal plane betatron oscillations, one with vertical, and one with synchrotron oscillations.

In order to test the effect of each sextupole family, we injected two planar bunches (with particles offset from the closed orbit in, respectively, the x- and y-coordinates), and a bunch, whose particles had non-zero initial momentum offsets. Figure 7 shows the simulation results.

One can see that the parabolic term disappears when the corresponding sextupoles are turned on in each case, which is the expected effect; the remaining linear term is insensitive to the sextupole fields. Currently, we don't exactly know its source.

3.2.5. *Decoherence in an imperfect lattice*

There exists another approach to suppressing spin decoherence: the spin wheel measurement method. [6] The basic idea there is to insert a solenoid generating a radial magnetic field into the (ideal) beamline. The beam particles' spin vectors precess incoherently in the horizontal plane – the cause of horizontal plane decoherence. A sufficiently high solenoid field will precess them

coherently in the vertical plane. The coherent precession is then assumed to be the dominant one, hence the conclusion that decoherence is suppressed.

The purpose of the following simulation is to show two things: *a)* that the spin wheel technique does not suppress decoherence, *b)* that the sextupole fields technique still does even in an imperfect lattice.

In the simulation we used an imperfect lattice, with imperfections introduced in the same way as in section 3.1.2. Because of imperfections, a radial magnetic field exists, that simulates the introduction of a SW-driving solenoid into the beam line.

Thirty particles were distributed uniformly in the vertical plane at injection. We tracked this beam through the lattice for $20 \cdot 10^6$ turns (20 seconds). Every $2 \cdot 10^4$ turns particles' spin vector components were recorded, and their dispersion (estimated as the standard deviation) was used as a decoherence measure. In Figure 8 are shown the dispersions for the radial and vertical spin vector components, when the sextupoles are turned off. Figure 8a shows the dispersion for the radial component, and we see that it goes up and down within bounds but does not accumulate (which is indicated by a statistically insignificant slope of the trend line labeled "slp"). This means that there is no spin decoherence in the horizontal plane when particle spin vectors precess in the vertical plane. However, if one turns to Figure 8b, one will observe the accumulation, as evidenced by the slope of the trend line being seven standard deviations removed from zero; meaning that decoherence just transferred from the horizontal, into the vertical plane.

As the next step we turned on the sextupole fields. The results are presented in Figure 9. We see that qualitatively nothing changed for the horizontal plane (except the dispersion bounds are a factor of 10 less), while in the vertical plane the accumulation trend vanished. Hence we conclude that the decoherence-suppressing effect of sextupole fields is plane-independent.

273 3.3. MDM faking signal

274 3.3.1. Problem statement

275 For this investigation, the primary cause for concern were machine imperfec-
 276 tions resulting from accelerator element tilts about the optic axis, because they
 277 induce a radial MDM angular velocity component, which precesses particle spin
 278 vectors in the same plane as the EDM, thus resulting in a faking signal.

279 The standard deviation of the distribution of the erroneous spin precession
 280 angular velocity component

$$\sigma [\Omega_x^{MDM}] = \frac{q}{m\gamma} \frac{G+1}{\gamma} \frac{\sigma [B_x]}{\sqrt{n}}, \quad (7)$$

281 where n is the number of imperfections contributing the radial magnetic field
 282 component B_x (or its equivalent E_y).

283 For the assessment of the capabilities of the frequency-based methodology,
 284 we need to answer two questions:

- 285 (1) Is the erroneous component independent of the particular element tilt
 286 angle distribution, i.e. is it a linear function $\Omega_x^{MDM} = L(\langle\theta_{tilt}\rangle)$ of the
 287 mean tilt angle?
- 288 (2) Is it (anti-)symmetric relative to time-reversal, i.e., $|\Omega_x^{MDM,CW}| = |\Omega_x^{MDM,CCW}|$?

289 What these questions add up to is: will the faking signal change sign, if we
 290 inject the beam in the opposite direction? If it does, since the EDM angular
 291 velocity will not, we can eliminate the faking signal from the final statistic.

292 We analyzed the same lattice, with the same way of introducing machine
 293 imperfections, as in the previous cases. In total, 11 simulations were done, in
 294 each of which we varied the tilt angle distribution's expectation value. Spin and
 295 orbital transfer maps were computed up to the third order Taylor expansion;
 296 in view of our spin decoherence suppression simulation results⁴ we were only
 297 looking at the behavior of the closed orbit particle. The injection energy is

⁴Meaning, when the sextupole fields are turned on, spin tune becomes independent of the particle trajectory, be it the closed or any of the betatron orbits.

298 270.0092 MeV (the precise FS energy for this lattice; i.e. the invariant spin axis
299 is radially-orientated).

300 3.3.2. Results and conclusions

301 *Results.* In Figure 10 is drawn the dependence of the spin precession angular
302 velocity vector's radial and vertical components on the mean E+B element tilt
303 angle distribution. We observe that regardless of the particular distribution,
304 all data points lie perfectly on the same straight line, which indicates a lack of
305 dependence on anything but the mean angle.

306 In Figure 11 are presented the relative differences between the clockwise
307 (CW) and counter-clockwise (CCW) beams' radial invariant spin axis compo-
308 nent and spin precession frequency at different mean E+B tilt angles. As before,
309 the non-zero average tilt angle is equivalent to the presence of a spin wheel driver
310 in the lattice. We varied the strength of the SW driver in two ranges: first in
311 a bigger one, then smaller. What we observed is that in both ranges the com-
312 pared variables have similar values for the CW vs CCW beams; in the case of
313 frequency, though, the similarity is the better, the higher is the SW driver's
314 strength (i.e. the faster the spin wheel is rolling).

315 We used Figure 10 to estimate what vertical spin precession frequency could
316 be expected as a result of misalignments. Assuming the number of misaligned
317 elements $n = 100$, and $\sigma[\theta_{tilt}] = 10^{-4}$ rad,⁵ we computed $\sigma[\langle\theta_{tilt}\rangle] = 10^{-5}$.
318 This gives us a confidence interval estimate, presented as Table 1. There's a
319 28% chance to encounter a $\Omega_x^{MDM} \in [50, 100]$ rad/sec.

Table 1: Probability to encounter an MDM-related EDM-faking singal less than Ω^{max}

Ω^{max} [rad/sec]	$P(\Omega_x^{MDM} < \Omega^{max})$
50	67%
100	95%

⁵We assume 10^{-4} to be the realistic element alignment precision.

320 *Conclusions.*

- 321 (1) We confirmed that the MDM component of the spin precession angular
322 velocity vector depends only on the expectation value, but not the form,
323 of the lattice's imperfection distribution,⁶ i.e. its *linearity*.
- 324 (2) We've observed some *asymmetry*, likely due to the difference between the
325 CW and CCW beams' closed orbits.
- 326 (3) The asymmetry is less pronounced at higher spin wheel roll rates.

327 4. Conclusions

328 With regard to systematic errors originating with the particle spin dynamics
329 in a storage ring, we came to the following conclusions:

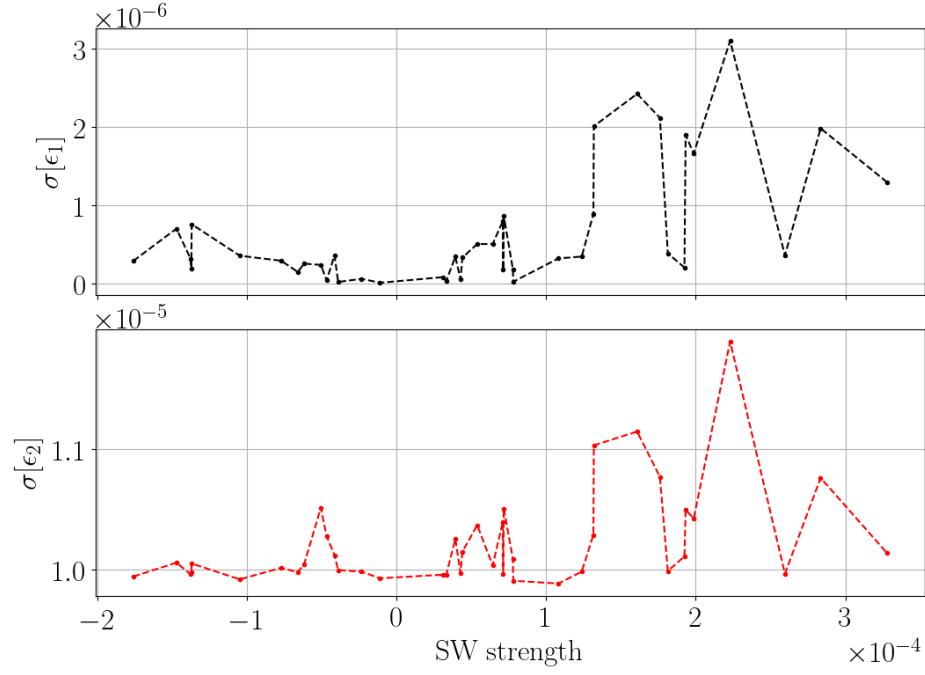
- 330 • The 2D Frozen Spin method's EDM statistic is robust with regard to
331 perturbations from the particles' betatron motion.
- 332 • Sextupole field spin decoherence suppression effect is independent of the
333 spin vectors' precession plane.
- 334 • The properties of the EDM-faking MDM signal are such as to
 - 335 – necessitate the use of a frequency-based methodology;
 - 336 – allow the exclusion of this signal from the final statistic.

337 References

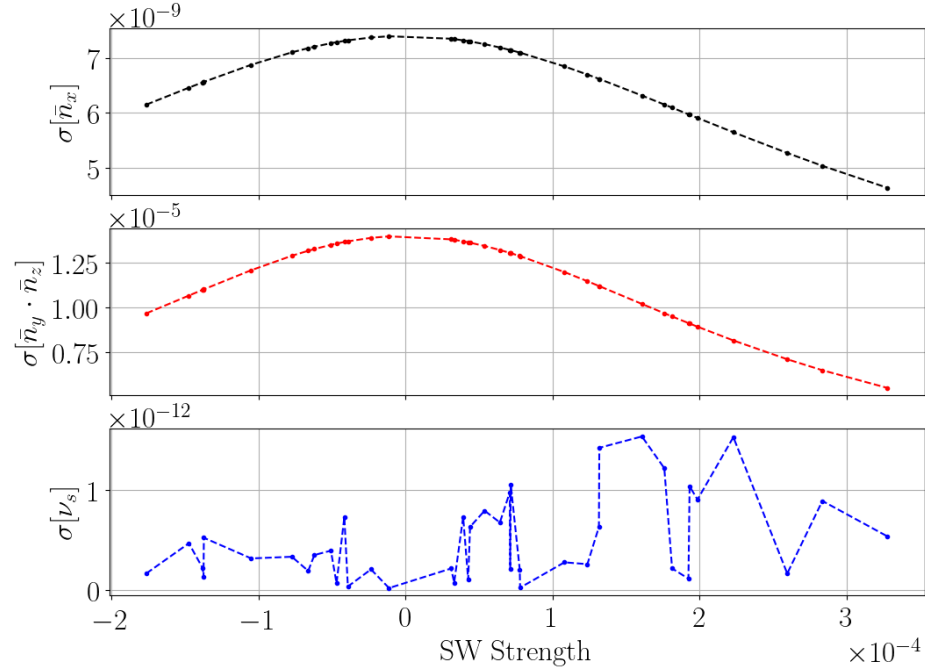
- 338 [1] A. D. Sakharov, JETP Lett.5(1967) 24.
- 339 [2] JEDI Collaboration. [http://collaborations.fz-juelich.de/ikp/jedi/](http://collaborations.fz-juelich.de/ikp/jedi/about/introduction.shtml)
340 [about/introduction.shtml](http://collaborations.fz-juelich.de/ikp/jedi/about/introduction.shtml)

⁶This has been confirmed only for the specific lattice we used, whose imperfections do not perturb the closed orbit.

- [3] Brown HN, Bunce G, Carey RM, Cushman P, Danby GT, Debevec PT, et al. Precise measurement of the positive muon anomalous magnetic moment. *PhysRevLett.* 2001;86:2227–31.
- [4] D. Anastassopoulos et al., “AGS Proposal: Search for a permanent electric dipole moment of the deuteron nucleus at the 10^{-29} e·cm level,” BNL, 2008.
- [5] Y. Senichev, A. Aksentev, A. Ivanov, E. Valetov, “Frequency domain method of the search for the deuteron electric dipole moment in a storage ring with imperfections,” arxiv:1711.06512 [physics.acc-ph] <https://arxiv.org/abs/1711.06512>.
- [6] S. Mane, “Spin Wheel,” arXiv:1509.01167 [physics] <http://arxiv.org/abs/1509.01167>.
- [7] A. Saleev et al., (JEDI Collaboration), “Spin tune mapping as a novel tool to probe the spin dynamics in storage rings.” *Phys. Rev. Accel. Beams* 20 (2017) no.7, 072801.
- [8] M. Berz, K. Makino, COSY INFINITY 10.0 Beam Physics Manual.
- [9] Y. Senichev, S. Andrianov, S. Chekmenev, M. Berz, E.Valetov. “Investigation of Lattice for Deuteron EDM Ring,” *Proc. of ICAP15 (2015)*. <http://accelconf.web.cern.ch/AccelConf/ICAP2015/papers/modbc4.pdf>.
- [10] Y. Senichev et al., “Spin tune decoherence effects in Electro- and Magnetostatic Structures.” *Proceedings of IPAC 2013, Shanghai, China*, pp. 2579-2581.
- [11] A. Aksentev, Y. Senichev, “Spin decoherence in the Frequency Domain Method for the search of a particle EDM,” presented at the 10th International Particle Accelerator Conf. (IPAC’19), Melbourne, Australia, May. 2019, paper MOPTS012.

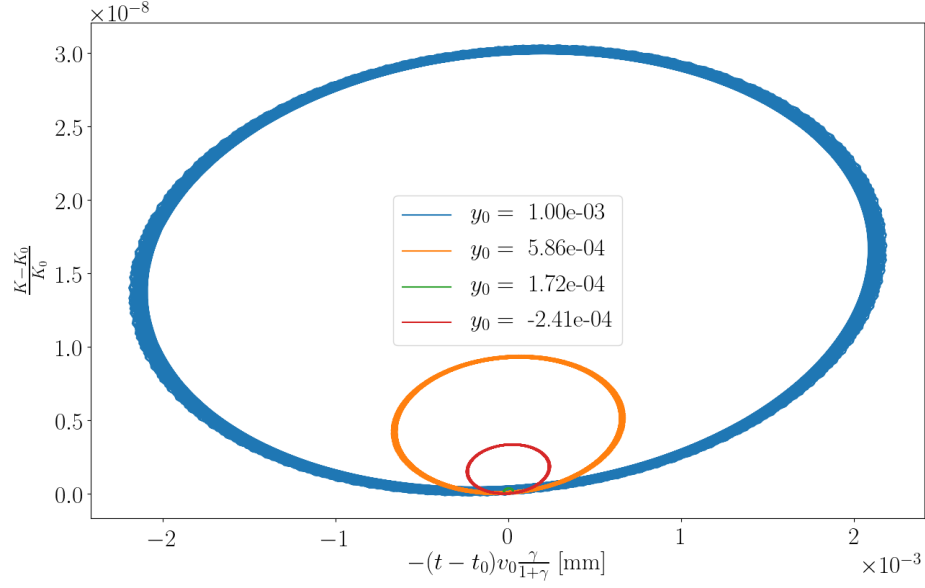


(a) Standard deviations of the comparator statistics versus the SW driver's relative strength.

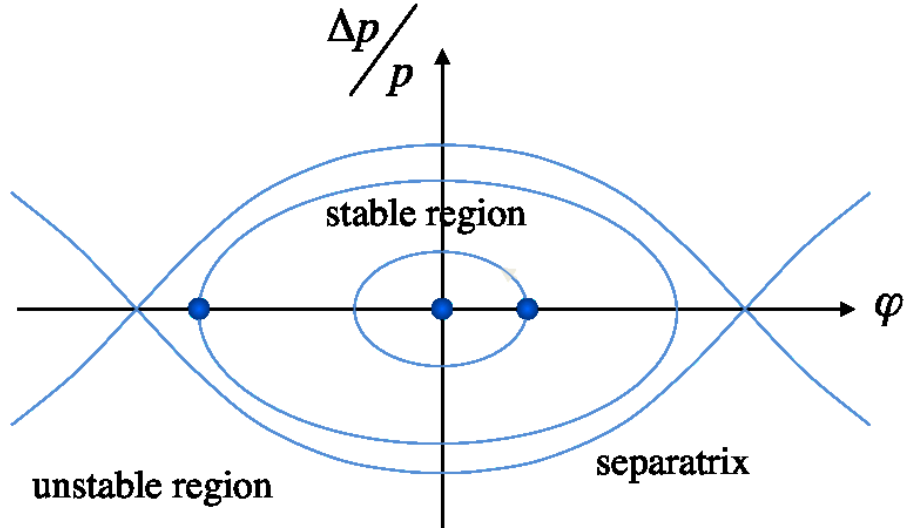


(b) The same statistic for the spin precession axis components and spin tune.

Figure 3: Effect of betatron oscillations on the particle spin dynamics simulation results.

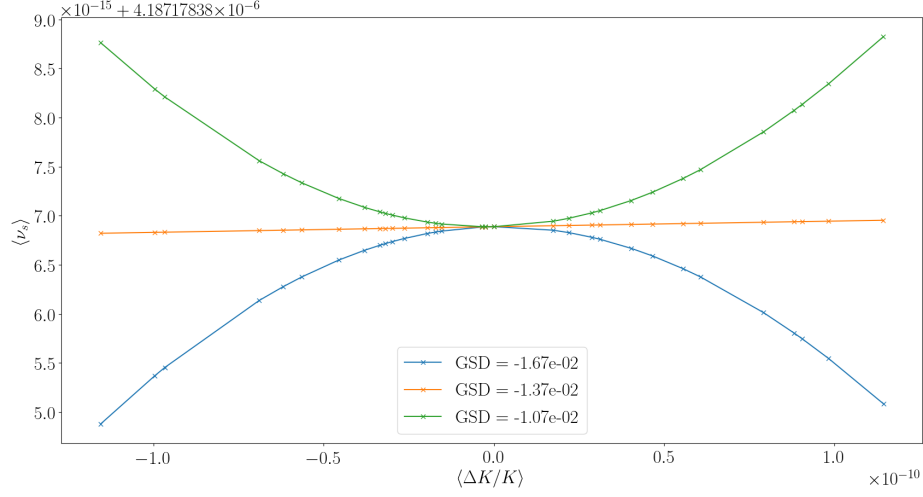


(a) Particles do vertical plane betatron oscillations. Colors mark the particles' vertical offsets at injection; all other initial coordinate offsets are zero. Third-order transfer maps were used in the computation of this plot's data.

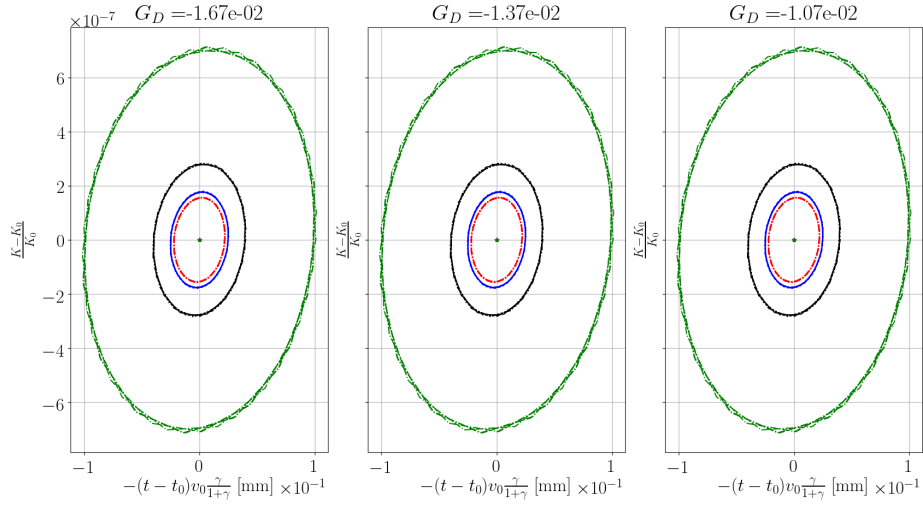


(b) Classic text-book image computed from a linear theory. All ellipses are centered on one point, i.e. all particles have the same equilibrium energy.

Figure 4: Longitudinal phase space portraits in a lattice using RF bunching.

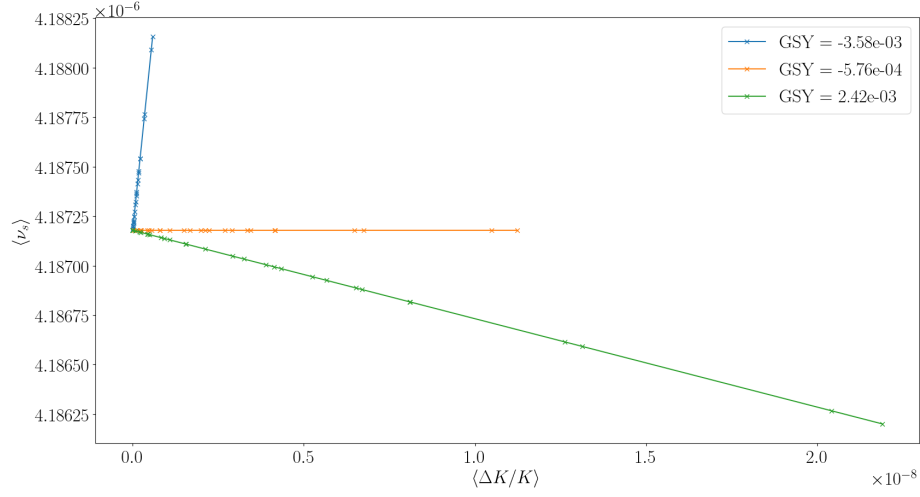


(a) Dependence of the mean level of a particle's spin tune on its mean energy level. Colors mark different sextupole field gradients. The functional form of the dependence changes with the field strength.

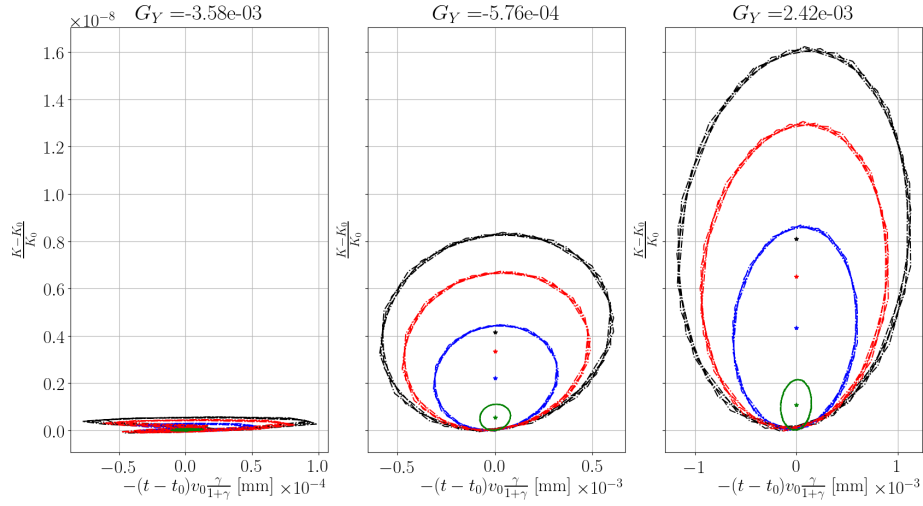


(b) Longitudinal phase space portraits of the injected particles. Particles were injected on the closed orbit, hence the sextupole fields do not affect their orbit length. No change is observed when the field strength changes.

Figure 5: Analysis of the sextupole fields' momentum compaction factor effect.

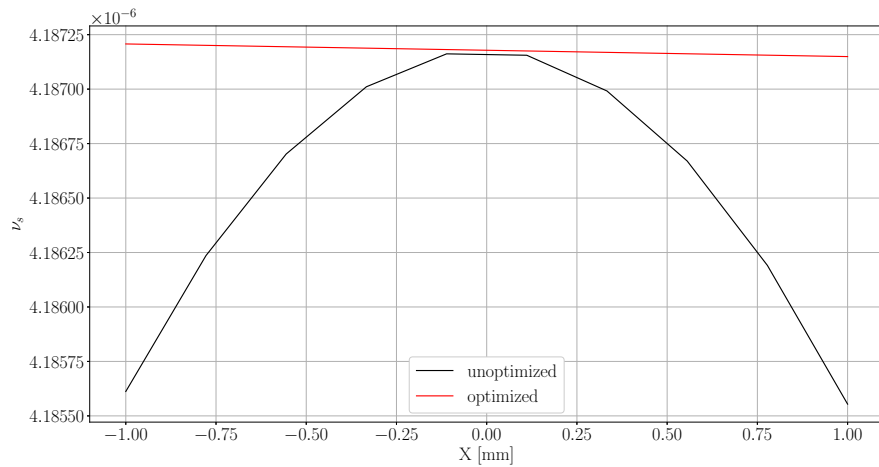


(a) Dependence of the mean level of a particle's spin tune on its mean energy level. Colors mark different sextupole field gradients. The functional form of the dependence changes with the field strength.

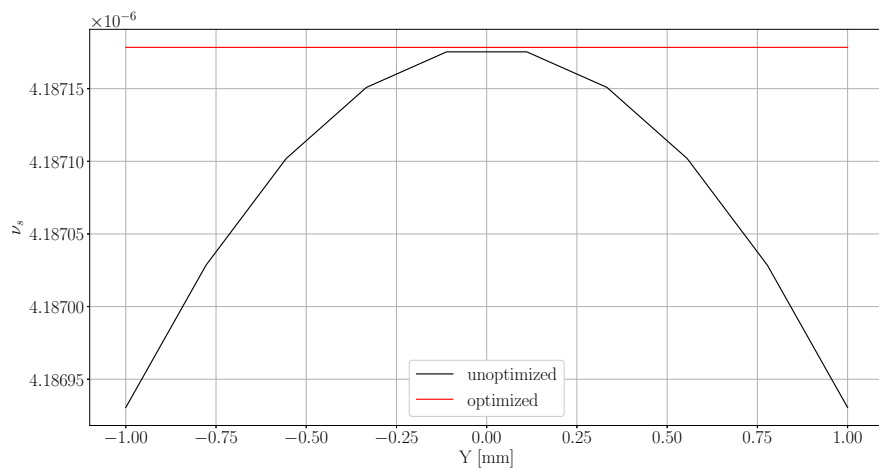


(b) Longitudinal phase space portraits of the injected particles. Particles were injected on different betatron orbits, hence sextupole fields modify their orbit lengths. Portraits compress when the fields strength is varied.

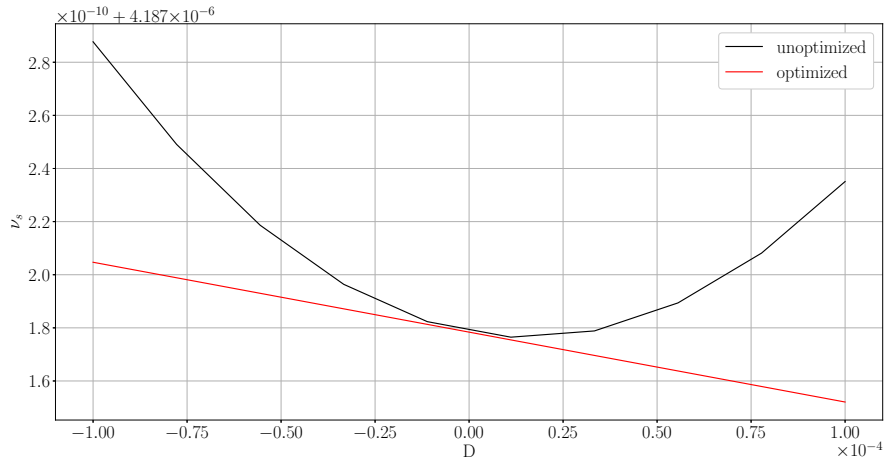
Figure 6: Analysis of the sextupole fields' orbit length effect.



(a) Horizontal plane betatron oscillations.

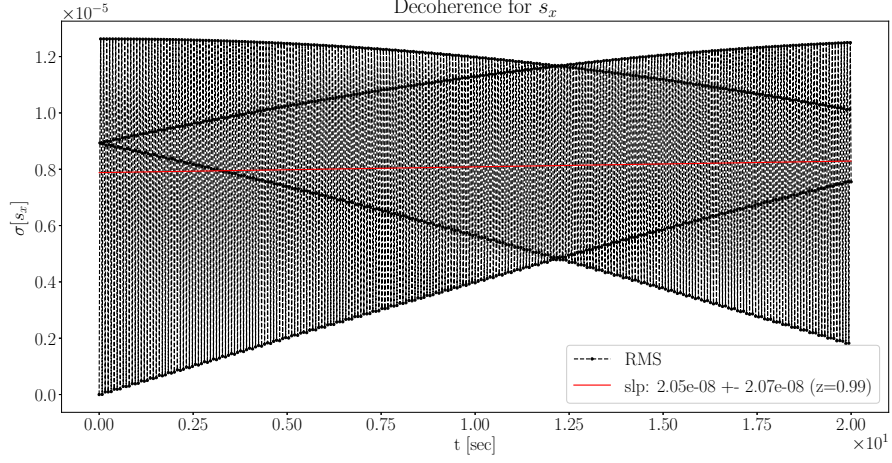


(b) Vertical plane betatron oscillations.

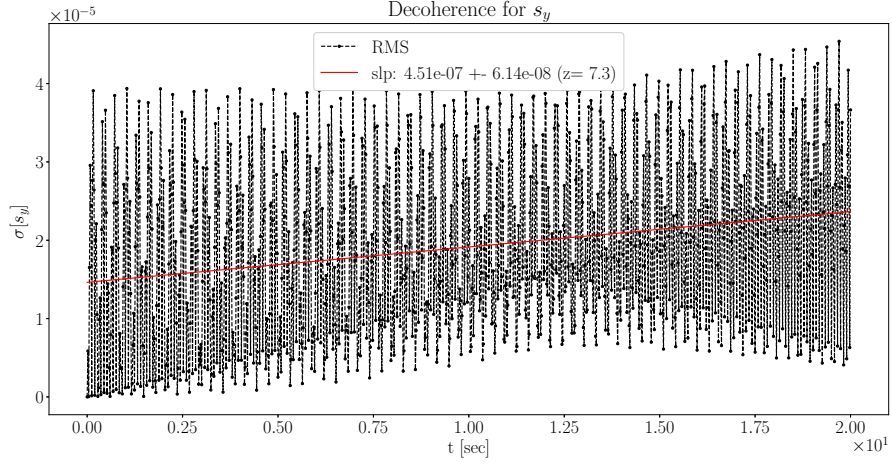


(c) Synchrotron oscillations.

Figure 7: Spin tune dependence on the initial particle offset from the reference value in one of the three phase space coordinates: X , Y , or $D \equiv \delta$. The black line represents that dependence prior to turning on the sextupole family responsible for the suppression of the corresponding decoherence type, red one after. We observe that in each case the parabolic term disappears when the sextupoles are turned on. The remaining linear term is insensitive to the sextupole fields.

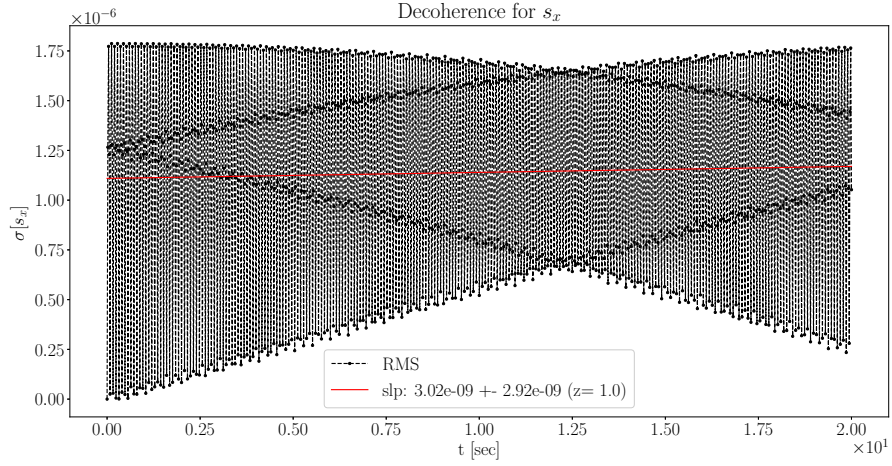


(a) Radial component distribution standard deviation.

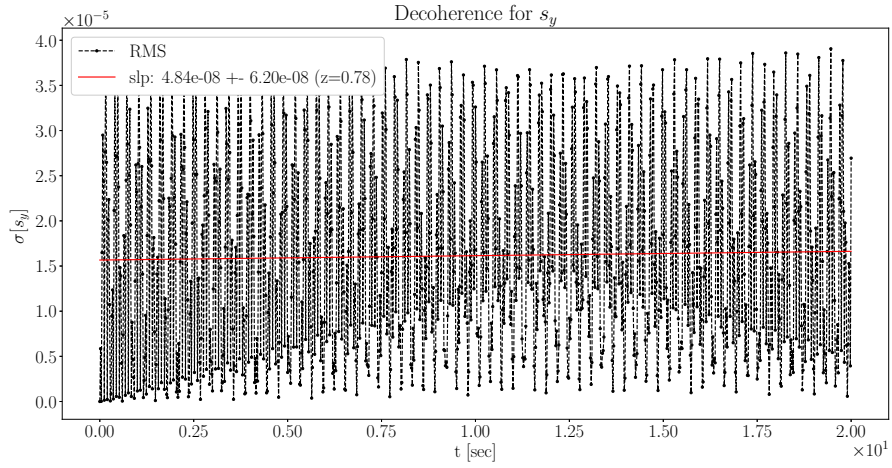


(b) Vertical component distribution standard deviation.

Figure 8: Standard deviation of the ensemble spin vector component distribution plotted against time. The standard deviation is used as a (local) decoherence measure. The red trend line is used to characterize the global decoherence behavior. We observe that the slope of the trend line is statistically insignificant in the case of the radial spin vector component, but is seven standard deviations removed from zero in for the vertical component. This means that there's no horizontal plane decoherence, but particle spin vectors disperse in the vertical plane. Sextupoles are turned off in this simulation.



(a) Radial component distribution standard deviation.



(b) Vertical component distribution standard deviation.

Figure 9: The same plots as in Figure 8, but in this case the sextupoles are turned on.

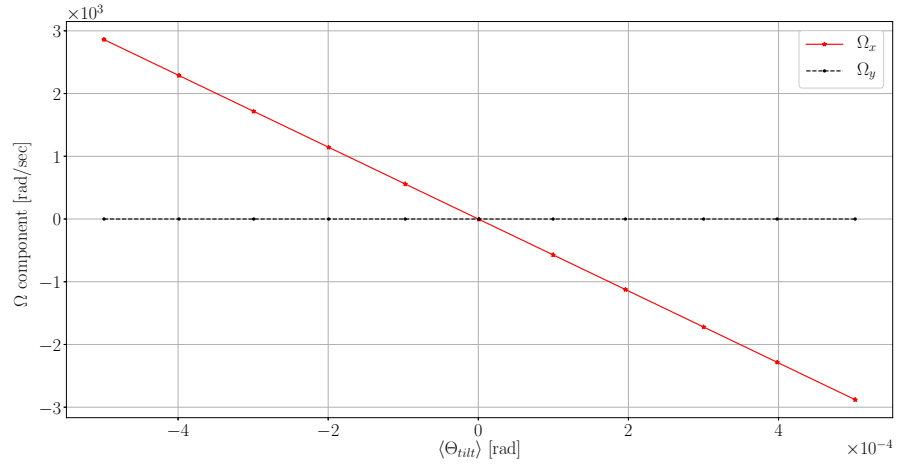
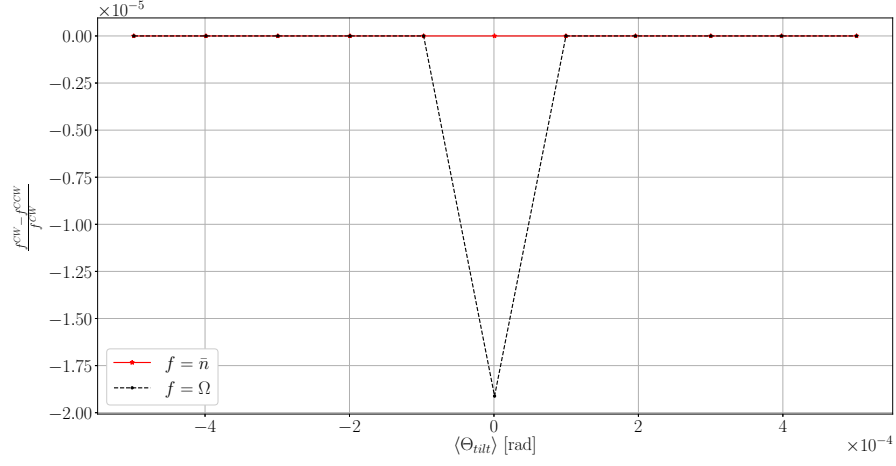
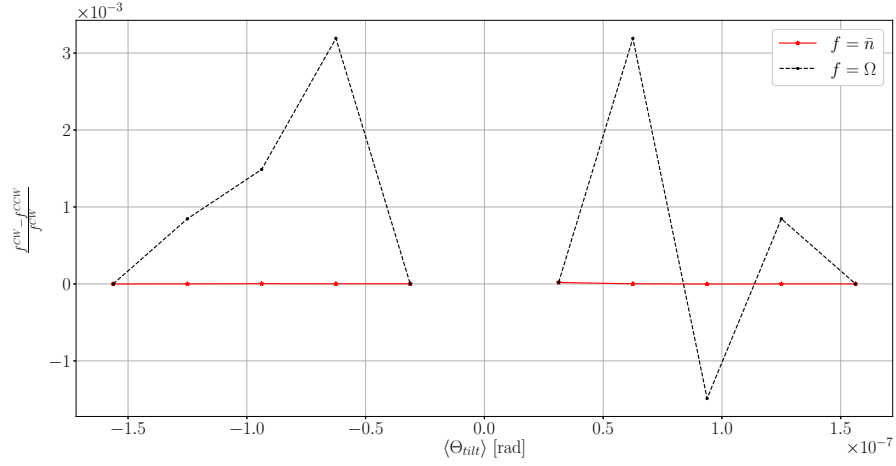


Figure 10: Components of the spin precession angular velocity vector for the reference particle plotted against the mean spin-rotator tilt angle. Each data point corresponds to a different tilt angle distribution; however, the vector components do not exhibit any pattern other than the linear dependence on the mean angle.



(a) Bigger SW driver strength range.



(b) Smaller SW driver strength range.

Figure 11: Relative difference between the clockwise and counter-clockwise beams' radial invariant spin axis component and precession frequency at different SW driver strengths. The compared variables are fairly similar; in the frequency case the similarity is the better, the greater the strength of the SW driver.